

Iterative Multiscale Computational Fluid Dynamics–Single-Particle Model for Intraparticle Transfer and Catalytic Hydrogenation Reaction of Dimethyl Oxalate in a Fluidized-Bed Reactor

Ya-Ping Zhu,[‡] Guo-Qiang Chen,[‡] and Zheng-Hong Luo^{†,*}

[†]Department of Chemical Engineering, School of Chemistry and Chemical Engineering, Shanghai Jiao Tong University, Shanghai 200240, People's Republic of China

[‡]Department of Chemical and Biochemical Engineering, College of Chemistry and Chemical Engineering, Xiamen University, Xiamen 361005, People's Republic of China

S Supporting Information

ABSTRACT: In this work, the coupled model based on an iterative approach was developed to describe the flow behavior and catalytic hydrogenation of dimethyl oxalate (DMO) in a fluidized-bed reactor (FBR). First, a single-particle model (SPM) and a computational fluid dynamics (CFD) model were constructed, respectively. A set of hyperbola-like kinetics equations were included in the SPM. Subsequently, we assumed that all catalyst particles inside each small computational cell for the CFD model experience the same external conditions, which ensures the effective coupling of the two models above. The assumption and the coupled model have been validated by evaluating the above assumption and comparing with the experimental data, respectively. Based on the validated model, the predictions of the two classical diffusion equations (i.e., the Wilke–Bosanquet diffusion equation and the Fick or Wilke diffusion equation) are compared. In addition, the main flow field and reaction parameters in the FBR were investigated numerically. The results indicated that the intraparticle transfer resistance rises with the increase of the particle size, while it is not obvious for the selected studied system. The results also indicated that all of the species mass fraction distributions become more even as the catalyst size becomes smaller and the different diffusion models have little influence on simulation results. The simulated results here also demonstrated that one is capable of investigating reactor behavior at relatively low computational cost by using the proposed multiscale model.

1. INTRODUCTION

1.1. Scope. The worldwide production capacity of chemicals via hydrogenation reaction (hydroprocessing) has been increased by several-fold from 2005 to now.¹ Among a family of hydroprocessings in refinery, the hydrogenation of dimethyl oxalate (DMO) becomes more and more important.² For instance, a green process for the production of ethylene glycol (EG), one of the most important alcoholic components, has recently been developed to convert coal to high-value-added chemicals, wherein one of the core reactions is the DMO hydrogenation.^{3–5}

Generally, the DMO hydrogenation reaction is performed over solid catalysts with high exothermicity.^{6–10} Since the DMO hydrogenation for producing EG is a gas–solid catalytic and exothermic reaction, a fluidized-bed reactor (FBR) is an appropriate reactor to produce EG via the DMO hydrogenation reaction due to its simple construction, excellent heat- and mass-transfer capabilities, and efficient mixing of reacting species.^{11,12} However, most of previous reports on the DMO hydrogenation reaction have been carried out in fixed-bed reactors.^{13–21} In addition, there have been few reports of the fluid dynamics in these reactors. The fluid dynamics is used to evaluate the reactor performances. In fact, a similar reaction such as the methanol to olefins (MTO process) was successfully carried out in FBRs.^{22,23} In view of the little investigation on the DMO hydrogenation in FBR, a two-phase computational fluid dynamics (CFD) model is developed

herein to describe the flow and DMO hydrogenation reaction in FBRs.

In a fluidized-bed catalytic hydrogenation reactor, the hydrogenation takes place on the surface of these catalyst particles (<1 mm) when they are exposed to the gas stream containing the reactants. It is a gas–solid two-phase reaction system.^{24–26} The gas phase consists of reactants, products, and byproducts; the solid phase consists of catalyst particles. In addition, these catalyst particles are generally spherical porous pellets within which the reactions occur.^{27,28} The internal diffusion which has a great influence on the reaction rates describes the molecular mass diffusion or molecular species transport through a fluid by the random and individual movements.²⁹ Accordingly, due to the coupling of diffusion and reaction, different length scales (multiscale) are involved in the DMO hydrogenation in FBRs (see Figure 1).³⁰ Detailed modeling of such a reactor is a challenging task, including the reactor design and accounting for complex gas–solid two-phase flow, particle–particle and particle–reactor interactions, intraparticle transfer, and nanoscale phenomena such as the kinetics of the active sites of the catalysts and molecular transport and collisions within particles.^{30,31} Therefore, to construct such a

Received: July 8, 2013

Revised: November 21, 2013

Accepted: December 12, 2013

Published: December 12, 2013

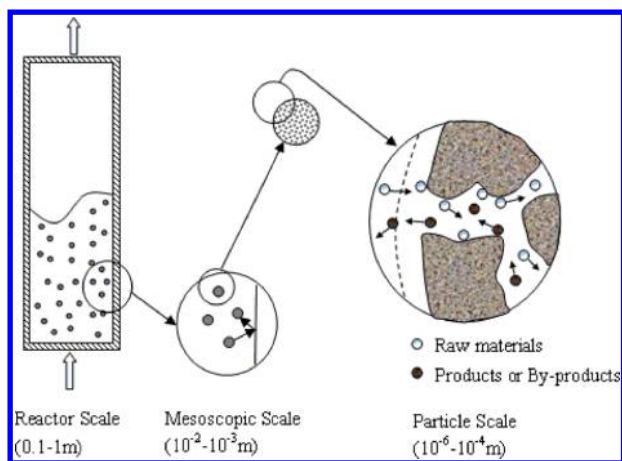


Figure 1. Multiscale phenomenon in the DMO hydrogenation process in FBRs.

detailed reactor model including all of the above factors is a very challenging task. A modern two-phase CFD model based on the Eulerian–Eulerian approach, namely, a multiscale CFD model, is needed to manage the above-mentioned complexities.

In this work, a multiscale model based on an iterative approach has been investigated using a two-phase CFD model coupled with a spherical porous pellet model (i.e., SPM) for the flow behavior and catalytic DMO hydrogenation reaction in a FBR. Intraparticle transfer and reaction are taken into account in the SPM. Since the geometries and the grids for the reactor are generated to solve the two-phase CFD model and these catalyst particles in the reactor are so small compared to the FBR, all catalyst particles inside each small computational cell for the CFD model have the same external condition to couple the SPM and the CFD model. This method is used to achieve novel understanding of FBRs employed in the catalytic DMO hydrogenation reaction field.

1.2. Summary of the Previous Works. CFD methods have been widely applied to gas–solid FBRs.^{32–43} In general, two different categories of CFD methods have been established to simulate gas–solid two-phase flow in FBRs, namely, the Eulerian and Lagrangian methods, respectively.^{32–35} For comparison between the two methods, the readers are encouraged to refer to refs 32–35. These previous CFD calculations for gas–solid flows are generally carried out under cold-flow conditions with ignoring of intraparticle transport and reactions. A porous pellet model, however, has to be incorporated into the CFD model in many gas–solid catalytic reactions as described above, which can be accomplished by combining a CFD model with a SPM.⁴⁴

Up to now, there have been two approaches for realizing the coupling of the CFD model and the SPM/the multiscale CFD modeling, namely, sequential modeling and iterative/concurrent modeling.^{45–47} Both approaches involve the hierarchy construction of numerical models operating at individual scales. Among them, the iterative multiscale model couples models at various scales allowing for the interaction between different scales iteratively.⁴⁵ Unfortunately, multiscale models developed so far are mostly sequential models and only a few are iterative ones. The simple iterative multiscale modeling uses the “weighting” method to correlate dominant mechanisms following the stability criterion for a steady structure in the FBRs.⁴⁷ However, numerous important physical processes such as the intraparticle transfer are ignored in the simple weighting

method. A classical mechanistic approach (i.e., the energy minimization multiscale approach, the EMMS approach) in which the variational criterion was formulated based on the evaluation of the compromise among interacting mechanisms was proposed and developed by Li et al.^{47,48} to implement an iterative multiscale CFD modeling.⁴⁹ To the best of our knowledge, however, there is so far no open literature on such iterative multiscale modeling approach in modeling the flow field in FBR for (DMO) hydrogenation reaction.

A number of single-particle models have been proposed for the gas–solid catalytic reactions^{28,50–55} Because the intraparticle transport is of the molecular mass diffusion or molecular species transport involving the random and individual movements (i.e., the molecular transport and collisions) in nature, and most molecular diffusion problems in chemical reactor processes involve transport of multi-component mixtures, these models are generally based on molecular diffusion models, which are employed to describe the diffusion fluxes.⁵⁵ There are four typical molecular diffusion models, namely, the Fick or Wilke model,⁵⁶ the Maxwell–Stefan model,⁵⁵ the dusty gas model^{57,58} and the Wilke–Bosanquet model.⁵⁵ Among them, the Fick or Wilke model and the rigorous Maxwell–Stefan model assume bulk diffusion, whereas the rigorous dusty gas model is used to describe the combined bulk and Knudsen diffusion fluxes. The Wilke–Bosanquet model is proposed to simplify the dusty gas model. In addition, a single-particle model to describe the mass and heat transport in a porous pellet with chemical reactions is formulated, based on one of these molecular diffusion models mentioned above with some simplifications or assumptions.^{59–62} For instance, following the above descriptions, Graaf et al.⁶⁰ used the dusty gas model to investigate the relative importance of Knudsen vs bulk diffusion for the methanol synthesis with ignoring of pressure gradient and the assumption of isothermal conditions throughout the spherical particle. Recently, Solsvik et al.⁵⁵ developed a comprehensive single-particle model for applying to two cases (the steam methane re-forming (SMR) and the methanol synthesis) in order to reduce and evaluate various molecular diffusion models. Mass diffusion fluxes were described according to the rigorous Maxwell–Stefan and dusty gas models, and the relatively simpler Wilke and Wilke–Bosanquet models.

The early modeling efforts in a gas–solid two-phase catalytic system are made to account for the detailed aspect of the CFD model and the SPM individually. In practice, the two are interlinked. The CFD and SPMs established before did not focus on the (DMO) hydrogenation reaction system yet.

2. ITERATIVE MULTISCALE CFD-SPM MODEL

In this contribution, a multiscale model based on an iterative approach is proposed via employing a SPM, a reaction kinetic model, and a two-phase CFD model altogether to describe the DMO hydrogenation in a FBR. Since the single-particle and two-phase CFD models were widely adopted in various gas–solid catalytic reaction systems, they have been briefly summarized in the Supporting Information (SI) section (see section SI-II of the Supporting Information for details).^{59,60,63–77} Herein, the kinetic model and the coupling mechanism for constructing the iterative multiscale model have been described.

2.1. Reaction Kinetics Model. With the fluid flow in the reactor, the DMO hydrogenation reaction occurs within the catalyst particles. Accordingly, the DMO hydrogenation

kinetics model is incorporated into the SPM via the reaction terms \mathcal{R}_i in eqs S1 and S3 of the Supporting Information. The kinetics model is applied in this study as described below.

The main reaction mechanisms are shown as follows:



where MG and EG are methyl glycolate ($\text{CH}_3\text{COOCH}_2\text{OH}$) and ethylene glycol ($(\text{CH}_2\text{OH})_2$), respectively. In this work, a hyperbolic-type kinetics model is used to describe the DMO hydrogenation kinetics based on the Langmuir–Hinshelwood model and the steady-state approximation, which was deduced in our previous work.⁶⁷ The kinetics equations applied in this work are given as follows:

$$\mathcal{R}_1 = \frac{k_1 K_{\text{DMO}} K_{\text{H}}^2 \left(P_{\text{DMO}} P_{\text{H}}^2 - \frac{P_{\text{MG}} P_{\text{CH}_3\text{OH}}}{K_{\text{P1}}} \right)}{\left(1 + K_{\text{H}} P_{\text{H}} + K_{\text{DMO}} P_{\text{DMO}} + K_{\text{CH}_3\text{OH}} P_{\text{CH}_3\text{OH}} + K_{\text{MG}} P_{\text{MG}} + K_{\text{EG}} P_{\text{EG}} \right)^3} \quad (3)$$

$$\mathcal{R}_2 = \frac{k_2 K_{\text{MG}} K_{\text{H}}^2 \left(P_{\text{MG}} P_{\text{H}}^2 - \frac{P_{\text{EG}} P_{\text{CH}_3\text{OH}}}{K_{\text{P2}}} \right)}{\left(1 + K_{\text{H}} P_{\text{H}} + K_{\text{DMO}} P_{\text{DMO}} + K_{\text{CH}_3\text{OH}} P_{\text{CH}_3\text{OH}} + K_{\text{MG}} P_{\text{MG}} + K_{\text{EG}} P_{\text{EG}} \right)^3} \quad (4)$$

where

$$P_i = 10^{-6} Y_i P \quad (5)$$

$$K_i = A e^{(-E_a/RT)} \quad (6)$$

The kinetics parameters were available based on the experimental data.^{68,69} More details regarding the experiments are reported elsewhere.^{68,69} The kinetics parameters are listed in Table 1 given in the Supporting Information.

2.2. Multiscale Model. As described earlier, in a gas–solid catalytic reaction system, chemical reactions generally occur within porous catalyst particles (i.e., intraparticle active sites). Reactants first enter into catalyst particles, and the products/intermediates undergo desorption and (external) diffusion to the gas phase. Generally, the pores of a catalyst particle are so small that these species come in or out of a particle mainly by slow diffusion. If the involved reactions are very rapid or strongly exothermic, an obvious influence of diffusion resistance will be detected. When the case takes place in a FBR, a coupled model/iterative multiscale model is required to describe both the intraparticle diffusion phenomenon and the fluid dynamic behavior in the FBR. Herein, the SPM, the reaction kinetics model (within the SPM), and the preceding CFD model are coupled to form an iterative multiscale model.

The coupling mechanisms are shown in Figure 2 schematically for the multiscale model developed. In simulation, after initialization, the pressure, temperature, and species mass fractions distributions in the FBR at the initial stage are set at first. Next, the continuity and momentum balance equations for the CFD model, i.e., eqs S18–S24 of the Supporting Information, are solved, and the information about the basic flow in each CFD numerical cell is obtained. Before the energy equations (i.e., eqs S25–S27 of the Supporting Information) and the species transport equation (i.e., eq S28 of the Supporting Information) for the CFD model are solved, the variables inside each CFD numerically established by solving

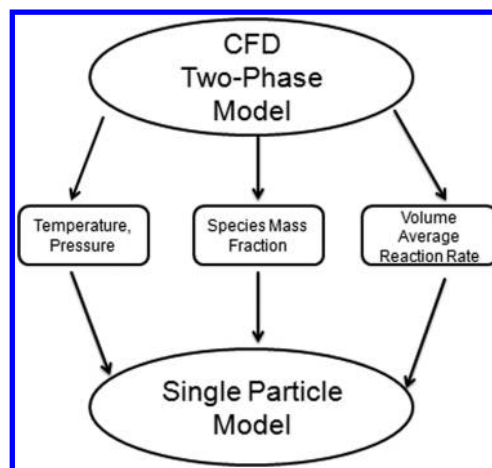


Figure 2. Couple schematic of the multiscale model.

the CFD model, namely, the pressure, temperature, and species mass fractions, are transferred into the SPM. As mentioned in the assumption for the coupling, the particles belonging to the same cell are subject to the same boundary conditions. Therefore, using these variables as the boundary conditions, the SPM is resolved in each cell to obtain the volume-averaged intraparticle reaction rates as well as the heat of chemical reactions, the source terms for the energy equations, and the species transport equation for the CFD model. Interactively, the preceding two variables are transferred into the CFD model to solve the energy equations and the species transport equations. Finally, the effect of intraparticle transfer should be considered to simulate the flow field in the FBR accurately. Thus, the SPM and the CFD model are coupled by the iterative approach. The solution program is executed in a loop with the above solution steps until the reaction time meets a given criterion.

The coupled model requires that the grid size inside a CFD model is fine enough, or the gradients of species mass fractions and temperature are small enough in a single grid, so that all particles inside the computational cell have the same external condition. For most situations this requirement is met as one cell is also the smallest unit that a CFD model could distinguish, which has been demonstrated in this work (see section 4).

3. SIMULATION CONDITIONS AND MODELING METHOD

3.1. Simulated Object. To validate the efficiency and accuracy of the iterative method for the multiscale simulation, we selected the lower part of a two-dimensional (2D) two-stage FBR (TS-FBR), which was reported in our previous works,^{62,73} as the simulated reactor (see Figure 3). In addition, the model parameters and boundary conditions were listed in Tables 1 and 2 of the Supporting Information.^{5,67,73,78} Unless otherwise noted, the parameters used for the forthcoming simulations are those in SI Tables 1 and 2.

3.2. Iterative Multiscale Modeling Method. The 2D simulations based on the multiscale model were performed with the industrial CFD code FLUENT 6.3.26 (Ansys Inc., Canonsburg, PA, USA) in the double precision mode. In addition, to simulate the 2D reactor, a commercial grid-generation tool, GAMBIT 2.3.16 (Ansys) was used to generate the 2D geometries of the reactor and the computational grids.

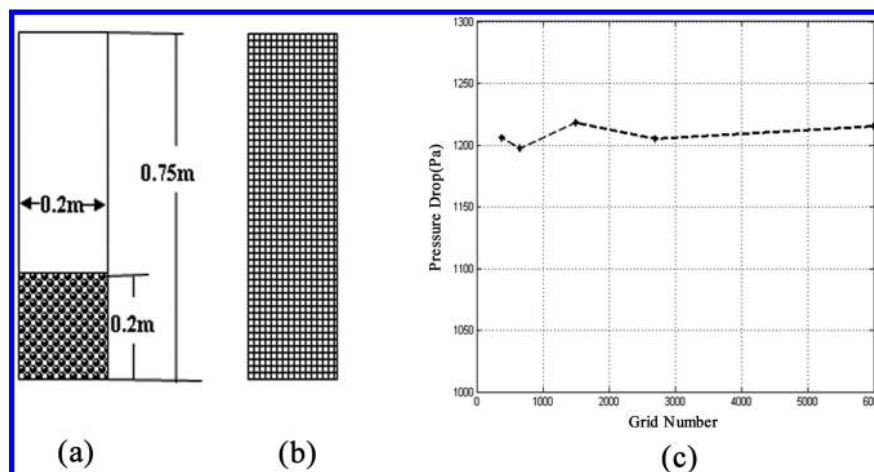


Figure 3. FBR configurations and grid independency: (a) reactor configuration; (b) CFD grid; (c) grid independency analysis.

The grid size sensitivity was examined initially, and the results indicated that a total amount of 75×20 uniform cells (each cell size is $0.01 \times 0.01 \text{ m}^2$; Figure 3) was adequate to conserve the mass of the solid phase for the entire FBR. This configuration was employed in the subsequent simulations. The governing equations in the CFD model were discretized into a uniform structural mesh by a finite volume method. All terms in the CFD model were discretized using a first-order upwind method. The pressure and velocity are coupled by the SIMPLE algorithm. The equations and the source terms of the SPM and the reaction kinetics model were incorporated into the CFD model via external user defined functions (UDFs). In order to simulate the practical cases, the results of the flow field without reaction and energy were first obtained. Then, the hydrogenation reaction and energy equations were simulated with the already obtained flow field. For the CFD simulations, the subrelaxation iteration method was used to ensure the simulations converged. The complete computation process is shown in Figure 4. The simulations were executed in a 2.83 GHz Pentium 4 CPU with 4GB of RAM.

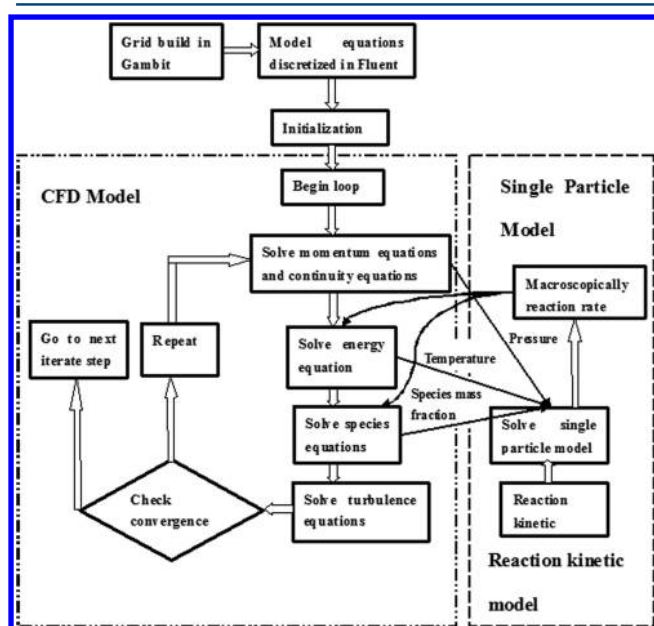


Figure 4. Flowsheet of the multiscale model solution.

4. RESULTS AND DISCUSSION

4.1. Intraparticle-Transfer Phenomena. In order to use the SPM accurately, the effectiveness factor is defined as the ratio of intraparticle reaction rate (i.e., macroscopic reaction rate) to the intrinsic reaction rate based on the average volume (see eq 7). If the intrinsic reaction rate is zero, the reaction effectiveness factor should be set to 1.

$$\eta = \begin{cases} \frac{\text{intraparticle reaction rate}}{\text{intrinsic reaction rate}} & (\text{at intrinsic reaction rate} > 0) \\ 1 & (\text{at intrinsic reaction rate} = 0) \end{cases} \quad (7)$$

Figure 5 shows the influence of the intraparticle heat-transfer limitation on the reaction. From Figure 5a, the intraparticle temperature gradient increased with the rise of the catalyst particle diameter. However, all of these gradients, including the maximal gradients between the particle outer surface and the particle center, are very small ($<1.5 \text{ K}$). Figure 5b demonstrates that reaction 2 is more sensitive to temperature change than reaction 1, while all of the simulated reaction rate changes are small ($<4\%$) as illustrated in Figure 5b. The heat-transfer Biot numbers (Bi_H) are at 0.0065–0.0080, which are smaller than 0.01.

Besides the intraparticle heat-transfer limitation, we also investigated the influence of the intraparticle mass-transfer limitation. The simulations were carried out by ignoring of the external diffusion, which has been proved in SI-III (see the Supporting Information). Figure 6 shows the intraparticle species mass fraction distributions at different particle diameters. Both the mass fractions of DMO and H_2 near the outer surface of particles were higher than those near the center, while the mass fraction distributions of Me, EG, and MG were to the contrary. Herein, the rate of reaction 1 was greater than that of reaction 2, which leads to MG as the intermediate product/reactant. In addition, Figure 6 shows that all of the species mass fraction distributions become more even with decreasing particle diameter. In practice, it is well-known that a smaller particle has a lower internal diffusion resistance.⁵⁷ The distributions of both rates of reactions 1-2 are also recorded to further describe the influence of the intraparticle mass-transfer limitation, as shown in Figure S1 (see section SI-IV of the Supporting Information for details), which resembles the shape in Figure 6. In summary, with the decrease of particle

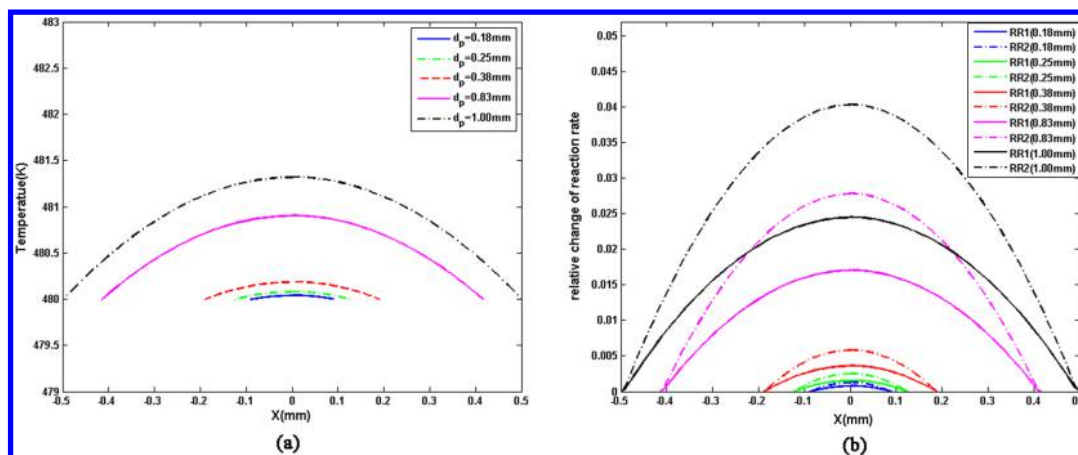


Figure 5. Intraparticle temperature distribution and its influence on the reaction rate: (a) temperature distribution; (b) relative change of both reaction rates caused by the temperature distribution. (Simulated conditions: $Y_{\text{DMO}}^s = 0.18138$, $Y_{\text{EG}}^s = 0.03018$, $Y_{\text{MG}}^s = 0.039526$, $Y_{\text{CH}_3\text{OH}}^s = 0.36052$, $Y_{\text{H}_2}^s = 1 - \sum_{i=1}^{N-1} Y_{i,j}^s$ and $T^s = 480 \text{ K}$.)

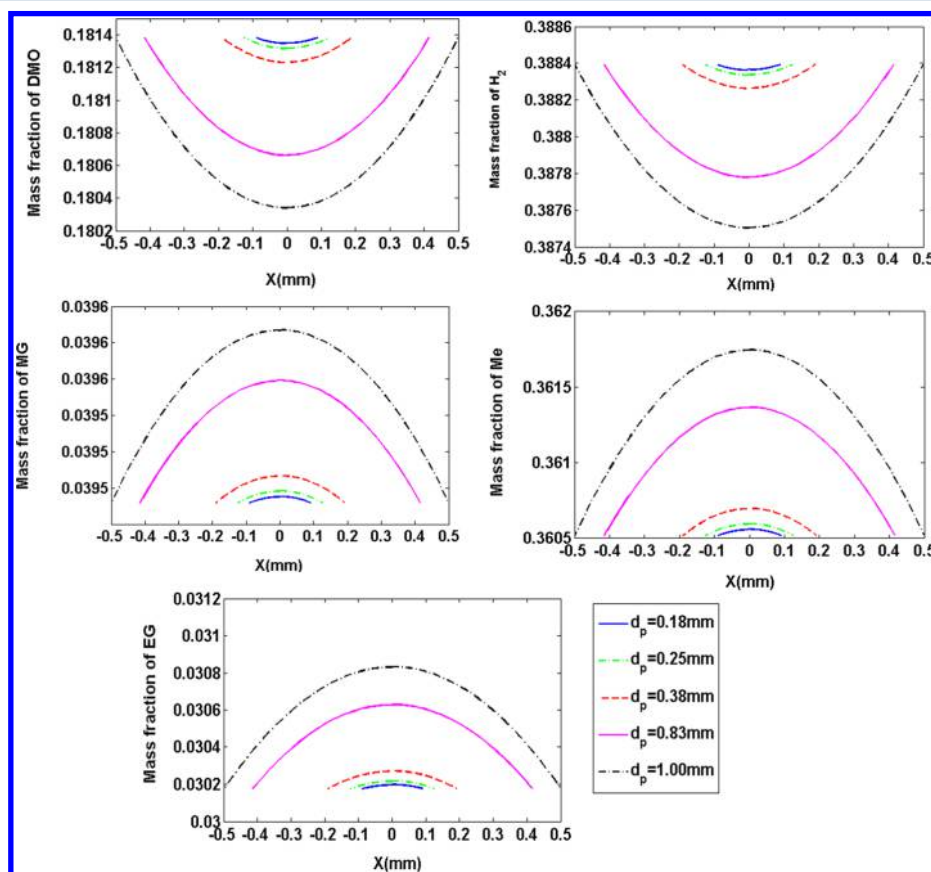


Figure 6. Intraparticle species mass fraction distributions: (a) DMO; (b) H_2 ; (c) MG; (d) Me; (e) EG. (Simulated conditions: $Y_{\text{DMO}}^s = 0.18138$, $Y_{\text{EG}}^s = 0.03018$, $Y_{\text{MG}}^s = 0.039526$, $Y_{\text{CH}_3\text{OH}}^s = 0.36052$, $Y_{\text{H}_2}^s = 1 - \sum_{i=1}^{N-1} Y_{i,j}^s$ and $T^s = 480 \text{ K}$.)

diameter, the effect as demonstrated in SI Figure S1 is similar to that shown in Figure 6.

Based on the SPM, the simulated results were also compared with certain experimental data from ref 69. Table 3 of the Supporting Information gives the comparisons between the experiment data from ref 69 and the simulations. The simulation results showed that the intraparticle DMO conversion decreased and both effectiveness factors for reactions 1 and 2 increased yet with the reducing particle size, which is consistent with the result from ref 69. The

obtained two effectiveness factors were greater than 0.999, when the simulated particle diameter was smaller than 0.38 mm, consistent with the experimental data. As a whole, the qualitative trends predicted by our simulation shown in SI Table 3 are in agreement with the results obtained from Zhang et al.'s experiments.⁶⁹

4.2. Validation and Evaluation of the Multiscale Model. Currently, there are no sufficient experimental data on cold flow conditions for the FBR to verify the flow behavior before implementing the hydrogenation reaction. However, it is

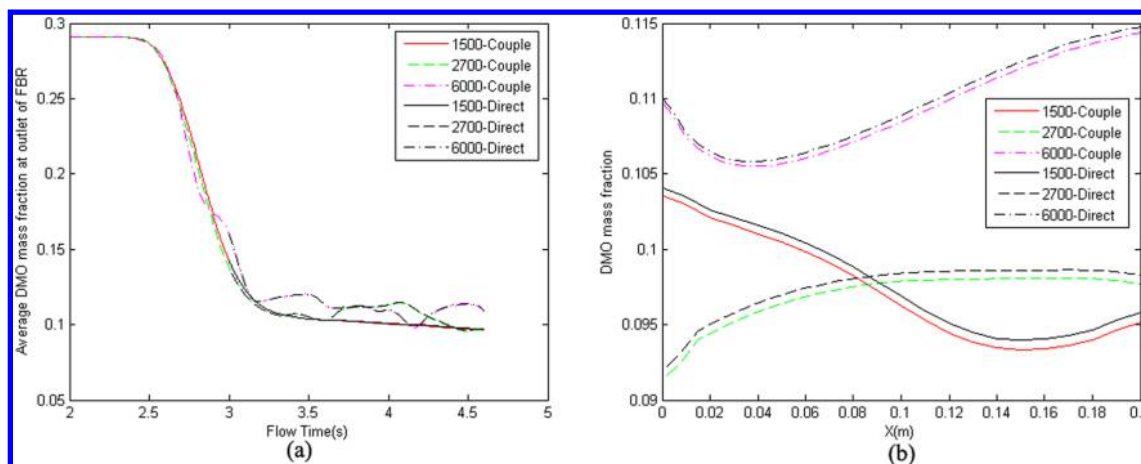


Figure 7. Mass fraction of DMO at different cell sizes: (a) average value changed with flow time; (b) distribution at the outlet of the FBR.

expected that the particle properties should have significant effects on the bed hydrodynamics. The KTGF (kinetic theory of granular flow) based on the two-fluid model with the Gidaspow drag model can successfully simulate the hydrodynamics of gas-fluidized beds, especially for the Geldart B- and D-type particles.⁷⁹ In this work, the catalyst particles exactly belong to the Geldart B-type, which means that our model should be valid to some extent.

Both the single-particle model and the two-phase CFD model are standard and have been validated in many open works.^{33–36,48,54–57} In this work, the only indeterminacy of the multiscale model is the coupling between the two classic models. The requirement to ensure the successful coupling between the two classic models is that the grid size inside a CFD model is fine enough, or the gradients of species mass fractions and temperature are small enough in a single cell. Therefore, if the above requirement is proved, the multiscale model should be effective. In order to validate this requirement, we obtained and compared the simulation results under different cell sizes (i.e., 0.01×0.01 , 0.0075×0.0075 , and 0.005×0.005 m²) via the multiscale model. The simulation results are shown in Figure 7, where the notation of “Couple” represents the simulation results obtained via the multiscale model, while the notation of “Direct” means simulation results obtained via the standard CFD model.

Figure 7a shows the average DMO mass fraction at the outlet of the FBR changes with time. The DMO mass fraction becomes stable after 4.0 s, which indicates that the reaction in the FBR is becoming stable. In addition, the fluctuation of the DMO mass fraction becomes greater with the increase of the total number of grids, which may be due to numerical dissipation. The DMO mass fractions under three different cell sizes become closer to each other. This indicates that all of the three grids can capture reaction performance in the FBR accurately. Figure 7b describes the DMO mass fraction distribution at the outlet of the FBR under the above three cell sizes. Though the DMO mass fraction distributions are different under the three cell sizes, the predicted difference between the couple model and the direct standard CFD model, which is due to transfer diffusion, is essentially the same. This indicates that the cell size of 0.01×0.01 m² is fine enough to describe the transfer resistance in a FBR. As a whole, Figure 7 demonstrates that the requirement for the coupling of the two models has been achieved, and thus, the multiscale model is effective at the selected cell size (0.01×0.01 m²).

A set of experimental data from our group was applied to validate the multiscale model. The simulated and experimental data were listed in Table 4 of the Supporting Information. SI Table 4 proves that the simulated data agree well with the experimental data. For the main products in the reaction system, all of the relative errors between experimental data and the simulation results via the multiscale model are less than 10%. In addition, from SI Table 4, the total mass percentage for all species shown in SI Table 4 obtained via experiment is less than 100%. It means that there is still byproduct in the reaction system.

The pressure drop is used to describe the gas and solid interaction in a FBR and evaluate the effectiveness of model parameters. A classical equation can be used to obtain the pressure drop, which is shown as follows:^{80,81}

$$\Delta P = (1 - \alpha_g)h_{mf}(\rho_s - \rho_g)g \quad (8)$$

All of the pressure drop data calculated via the classical equation, the SPM, and the pure CFD model are shown in Figure 8 which shows the bed pressure drop profile as a

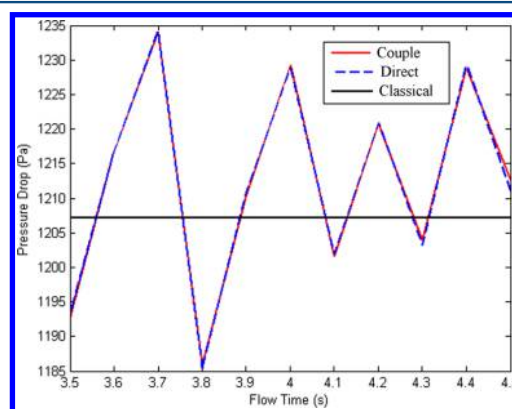


Figure 8. Pressure drop in FBR with the fluidization proceeding.

function of the flow time in the FBR. From Figure 8, both simulated values are fluctuant based on the classical calculated values. The relative error between the simulated values via the multiscale model and the classical calculated values is less than 2.3%. The simulated data of the pressure drop are in agreement with the classical calculated data. In addition, the simulated pressure drop values using the multiscale model and the pure

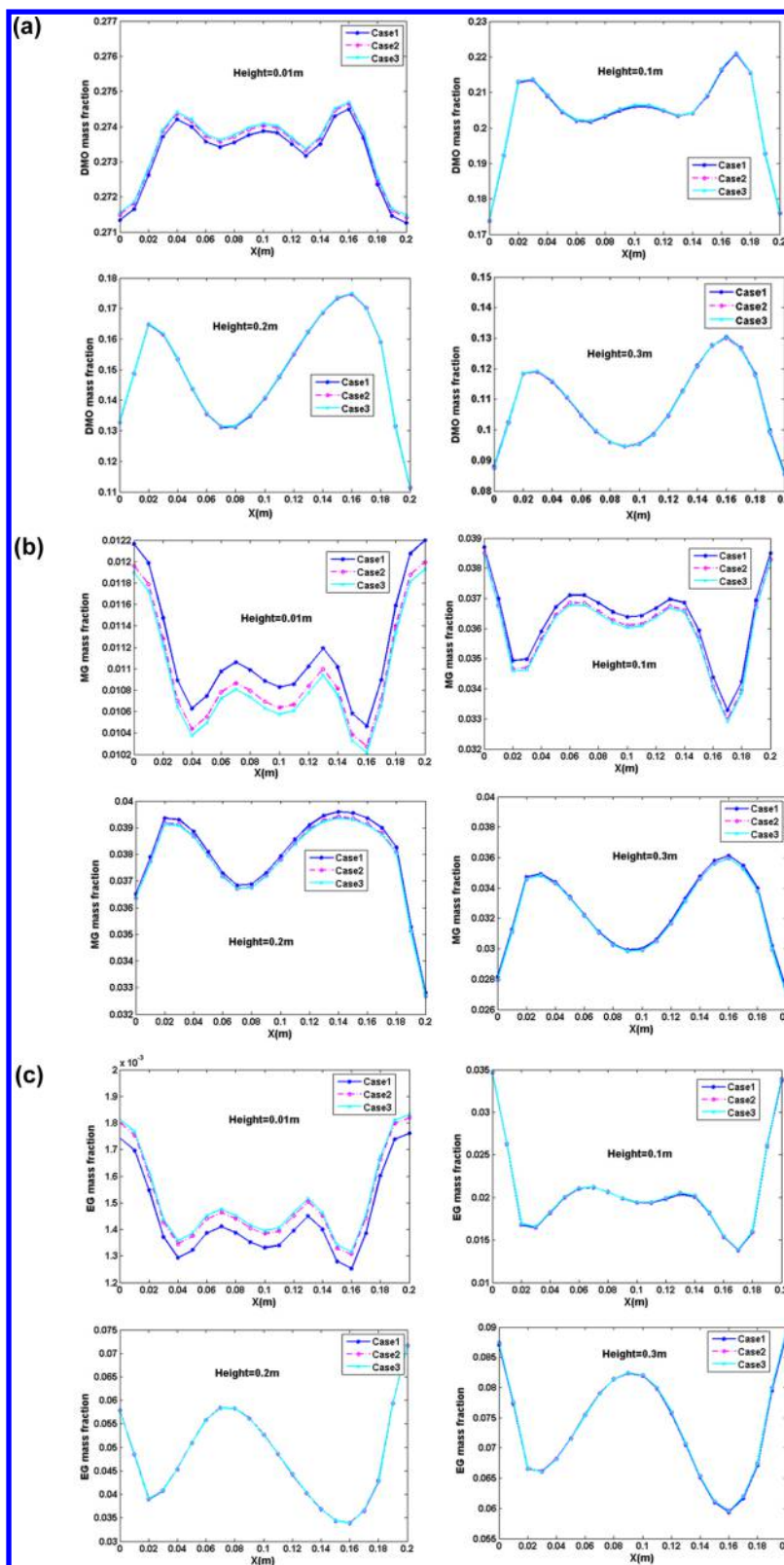


Figure 9. Radial mass fraction distributions of main species at different heights of the FBR: (a) DMO; (b) MG; (c) EG.

CFD model are nearly the same (Figure 8). In practice, the intraparticle-transfer limitation has little effect on the bed pressure drop. Accordingly, compared with the pure CFD model, the incorporating of the SPM to form the multiscale model has small effect on the calculation of the bed pressure

drop. As a whole, Figure 8 further demonstrates that the multiscale model is effective for simulating a FBR.

In addition, the Wilke and Wilke–Bosanquet diffusion models, which are typical for describing the intraparticle diffusion phenomena, have been incorporated into the multiscale model respectively to make comparisons. Here,

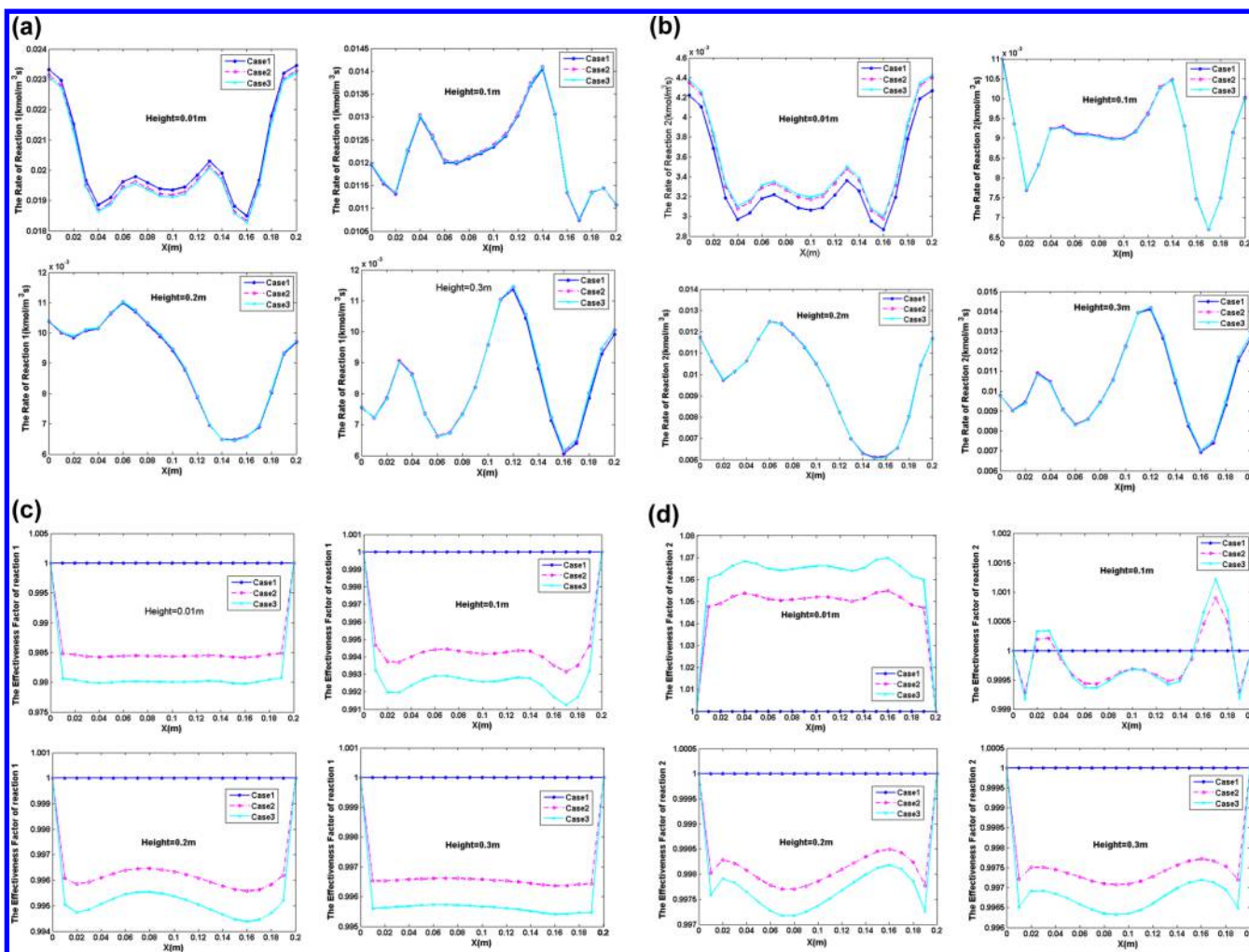


Figure 10. Radial reaction rate distributions and radial effective factor distributions at different heights of the FBR: (a) R1 (reaction 1); (b) R2 (reaction 2); (c) Yita1 (which refers to the effectiveness factor for reaction 1); (d) Yita2 (which refers to the effectiveness factor for reaction 2).

three cases involving the CFD model coupled with the reaction kinetics model (case 1), the multiscale model with the Wilke diffusion model (case 2), and the multiscale model with the Wilke–Bosanquet diffusion model (case 3) have been investigated. In addition, the small differences between the simulated results obtained from these different cases are shown in line-type plots.

Figure 9 shows the main species mass fractions at different FBR heights. There are major differences at the bottom part of the FBR for the three cases. The differences become smaller along the flow direction in the FBR for the three cases, which is related to the stability in the FBR. Compared with those for case 1, both of the reaction rates of reactions 1 and 2 for cases 2 and 3 are lower at the FBR bottom, and less raw materials are consumed, resulting in higher mass fractions of raw materials. With the gas flowing up, higher mass fractions of raw materials lead to higher reaction rates, resulting in greater consumption of the raw materials. In addition, Figure 9 also illustrates the differences of the main species mass fractions at the radial direction in the FBR bottom are not large for cases 1–3. The above results prove that the fluidization is effective at the FBR bottom. There are two rising bubbles from the bottom bed to the top that contribute to the two peaks.

Figure 10 shows the reaction rates and their effectiveness factors for cases 1–3, and there are still major differences at the

FBR bottom for the three cases, while the effectiveness factor at the bottom part of the FBR is great by 2% and then reduces to <1% for cases 2 and 3, which indicates the intraparticle diffusion effect is not great.

As a whole, for case 1, because the intraparticle-transfer limitation has been ignored, many intraparticle details cannot be predicted. Figures 9 and 10 demonstrate that the simulated difference between cases 2 and 3 is small, meaning that different diffusion models have little influence on the simulation results. Since the other parameters such as the pressure, the temperature, and the solid volume fraction are too close to compare for cases 1–3, the results are not listed herein. The following simulations will be carried out, based on case 2 only.

4.3. Application of the Multiscale Model. Since the particle diameter plays the key role on the intraparticle-transfer limitation and the inlet gas velocity may reflect the external-transfer limitation, their influences on the flow field in the FBR are meaningful and have now been predicted by the multiscale model based on case 2. In case 4, the particle diameter is changed to 0.38 mm. In case 5, the inlet gas velocity is changed to 0.3 m/s and the particle diameter is changed to 0.38 mm.

The catalyst volume fraction distribution became more uniform with smaller catalysts in the FBR, as shown in Figure 11. As particle diameter decreases, the maximum value of the catalyst volume fraction decreases. This indicates the fact that

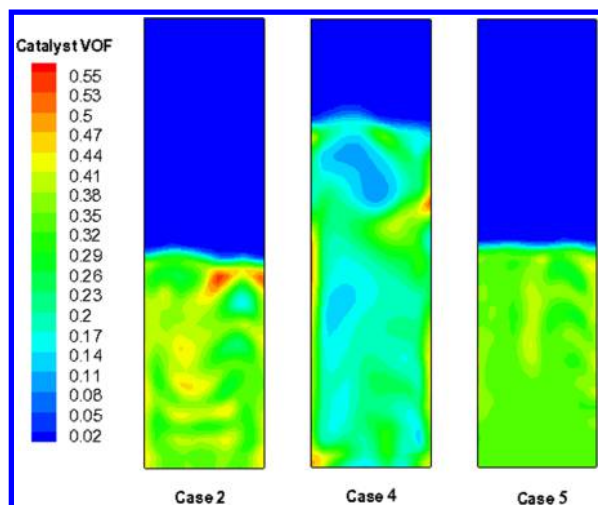


Figure 11. Transient catalyst volume fraction distribution at $t = 4.6$ s in the FBR. (Simulation conditions: (case 2) $v_g = 0.6$ m/s, $d_p = 0.83$ mm; (case 4) $v_g = 0.6$ m/s, $d_p = 0.38$ mm; (case 5) $v_g = 0.3$ m/s, $d_p = 0.38$ mm.)

mingling of raw materials and catalyst particles is improved and less gas passes through the FBR in the form of bubbles. Comparing case 4 with case 5 in Figure 11, one knows that the

expansion ratio of the fluidized bed decreases and the catalyst volume fraction increases with the reduction of inlet velocity. In practice, both the particle diameter and the inlet gas velocity have important influences on the flow field of a FBR, which are reflected in the CFD model equations (i.e., SI eqs S18–S55).

The reaction rate distributions and effectiveness factor profiles are described in Figure 12. The rate of reaction 1 decreased along the flow direction in the FBR, while, due to the reason that reaction 2 took place in sequence with reaction 1, the rate of reaction 2 has a maximum value in the middle region of the FBR. In addition, Figure 12 also shows that the effectiveness factor increases obviously with the decreases of particle size, and the effectiveness factors become close to 1.0 when the particle diameter is reduced to less than 0.38 mm. In practice, smaller particles lead to small intraparticle diffusion limitations. Due to computational error, the effectiveness factor at about 1 in case 5 for the FBR has some fluctuations. This is induced by the interplay of the dynamics of intraparticle species mass fraction and species mass fraction at the outer surface of catalyst particles caused by the reactions. However, the fluctuation of effectiveness factor at 1.0 in case 5 has little influence on the final simulation as it is very close to 1.0.

Figure 13 shows the main species mass fraction distributions in the FBR. The DMO conversion and EG selection increased slightly with the decreases of particle diameter. In practice, the decrease of particle diameter increases both the effectiveness

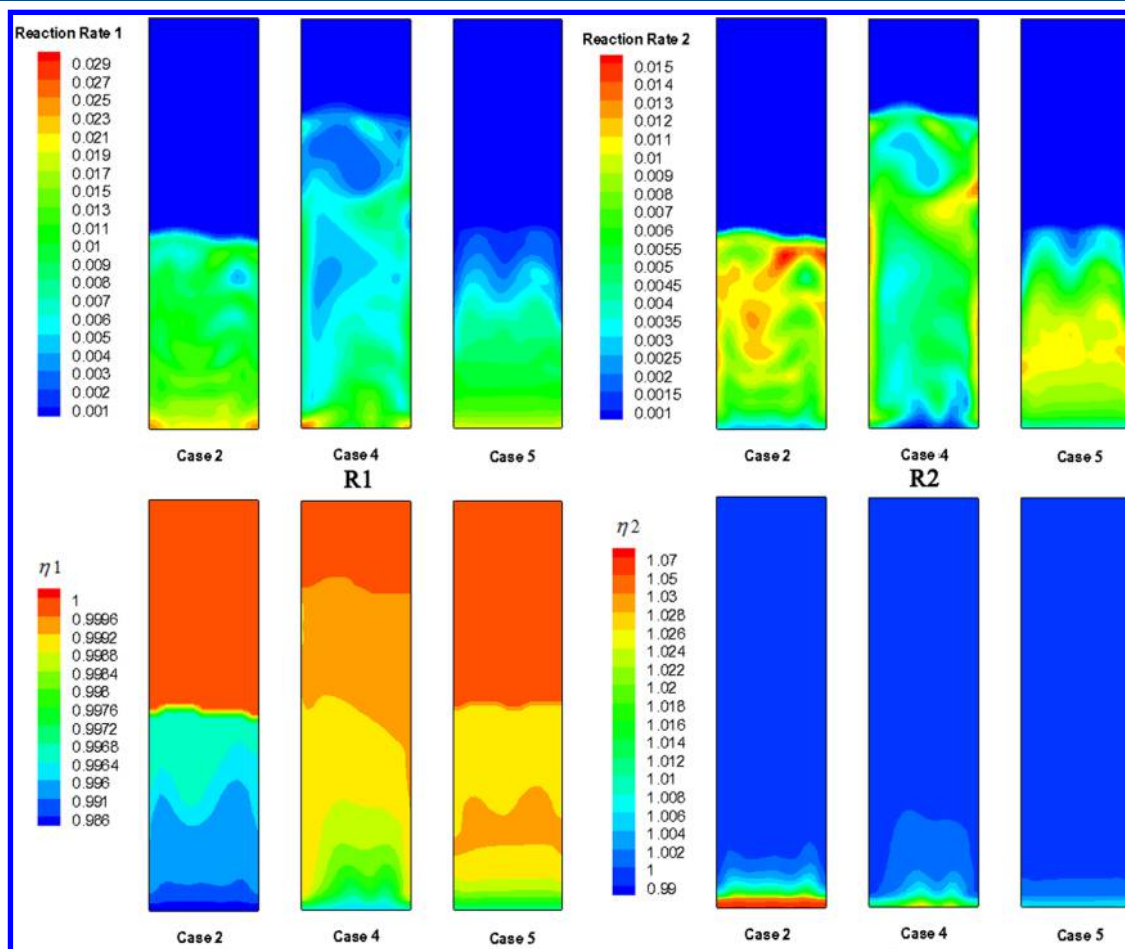


Figure 12. Transient reaction rate distributions and effective factor distributions at $t = 4.6$ s in the FBR. (Simulation conditions: (case 2) $v_g = 0.6$ m/s, $d_p = 0.83$ mm; (case 4) $v_g = 0.6$ m/s, $d_p = 0.38$ mm; (case 5) $v_g = 0.3$ m/s, $d_p = 0.38$ mm. In addition, R1 stands for reaction 1, R2 stands for reaction 2, η_1 stands for the effectiveness factor for reaction 1, and η_2 stands for the effectiveness factor for reaction 2.)

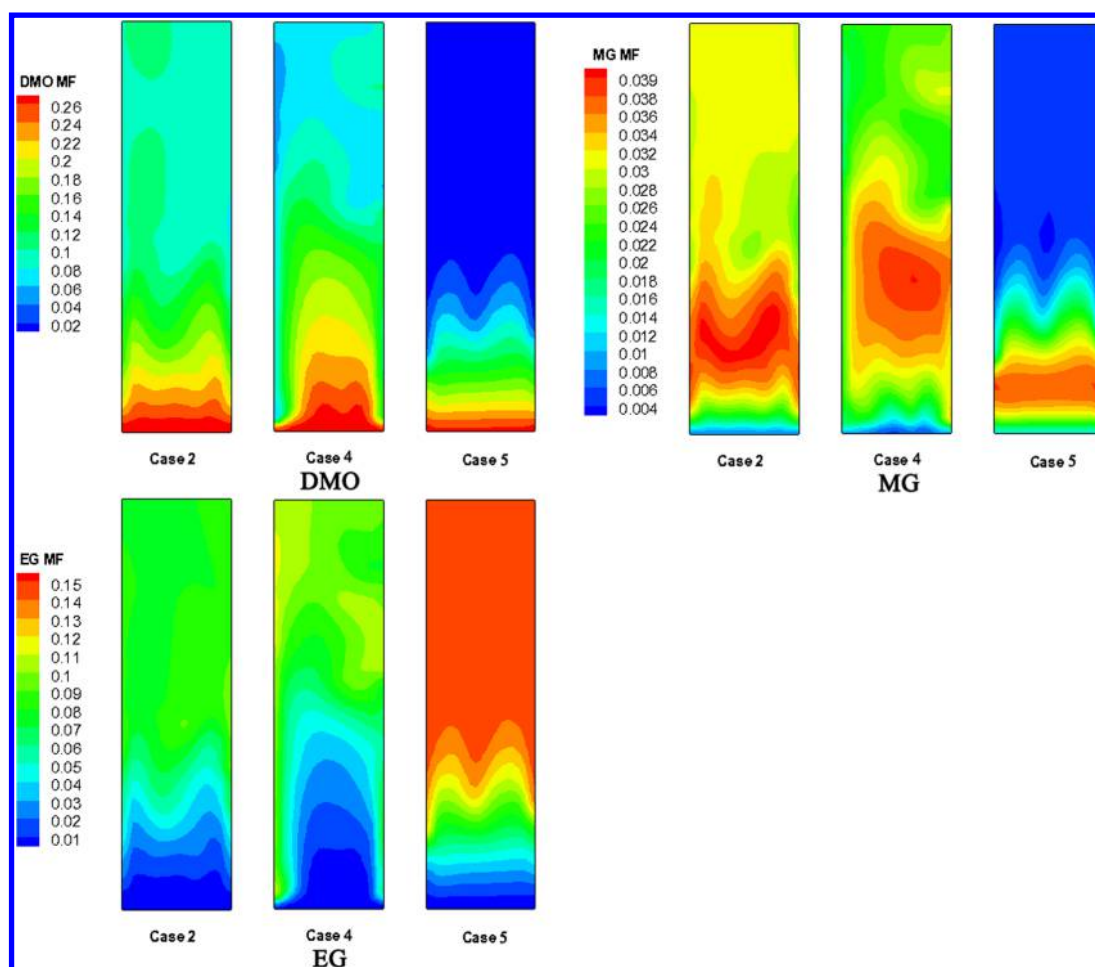


Figure 13. Main species transient mass fraction distributions at $t = 4.6$ s in the FBR. (Simulation conditions: (case 2) $v_g = 0.6$ m/s, $d_p = 0.83$ mm; (case 4) $v_g = 0.6$ m/s, $d_p = 0.38$ mm; (case 5) $v_g = 0.3$ m/s, $d_p = 0.38$ mm.)

factors and reaction rates. Such an increase is limited as all the particle diameters in practice are not large. Meanwhile, the DMO conversion and EG selection increase obviously, nearly by 50%, with the reducing inlet gas velocity. This is due to the increase in contact time between the gas reactants and the catalysts.

On the other hand, both the temperature distribution of the gas and the catalyst and the slip velocity in the FBR are recorded to further demonstrate the influences of the particle size and the inlet gas velocity. The detailed simulated results are given as Supporting Information (see section SI-IV of Supporting Information for details). In summary, the intraparticle mass-transfer limitation increases with the increase of the particle size, while the external-transfer limitation decreases with the increase of the inlet gas velocity.

5. CONCLUSION

In this study, a coupled model based on an iterative approach using a two-phase CFD model incorporating a SPM, i.e., an iterative multiscale CFD model, has been proposed to describe the flow behavior and catalytic DMO hydrogenation reaction in a FBR. A hyperbola-like kinetics model has been included in the SPM. The influences of two classical diffusion models (i.e., Wilke–Bosanquet model and Fick or Wilke model) have been investigated. The intraparticle-transfer phenomenon has been investigated using the SPM extensively. Both the SPM and the multiscale model are validated by comparing simulation results

with the experimental data. Furthermore, the requirement to achieve the coupling of the CFD model and the SPM for constructing the multiscale model is validated. Three case studies have been carried out: (i) by involving the CFD model coupled with the reaction kinetics model directly; (ii) with the multiscale model using the Wilke diffusion model; (iii) with the multiscale model using the Wilke–Bosanquet diffusion model. Finally, the complete model has been used to investigate the influences of mass-transfer limitations on the flow fields.

The simulated results show that the multiscale model describes appropriately the flow behavior and catalytic DMO hydrogenation reaction in a FBR. The intraparticle temperature gradient increases with the increase of the catalyst particle size. However, all these gradients are not large and may be ignored. Both the mass fractions of DMO and H_2 outside the particle surface are higher than those deep inside the particles, while the mass fraction distributions of Me, EG, and MG are to the contrary. All of the species mass fraction distributions become more even as the catalyst size becomes smaller. The different diffusion models (i.e., the Wilke diffusion model and the Wilke–Bosanquet diffusion) have little influence on simulation results. The proposed model and its solution method are helpful for the multiscale reactor modeling.

■ ASSOCIATED CONTENT

📄 Supporting Information

Tables listing kinetic parameters used, model parameters for the advanced model, simulation of the internal diffusion and experimental data, comparison between simulated and experimental data, and simulation of the external diffusion and experimental data, text giving the descriptions for the single particle and two-phase CFD models, the influence of the particle external diffusion, the supplementary simulation results, and accompanying references, and figures showing intraparticle reaction rates distribution, transient temperature distribution, and transient slip velocity distribution. This material is available free of charge via the Internet at <http://pubs.acs.org>.

■ AUTHOR INFORMATION

Corresponding Author

*E-mail: luozh@sztu.edu.cn. Tel.: +86-21-54745602. Fax: +86-21-54745602.

Notes

The authors declare no competing financial interest.

■ ACKNOWLEDGMENTS

We thank the National Ministry of Science and Technology of China (Grant No. 2012CB21500402), the National Natural Science Foundation of China (Grant Nos. 21276213 and 21076171), and the State-Key Laboratory of Chemical Engineering of Tsinghua University (Grant No. SKL-ChE-13A05). We thank Dr. Qiang Zhang (Tsinghua University) for his kind suggestions and meaningful contribution to the manuscript. We also thank the anonymous reviewers for the helpful comments on this manuscript.

■ NOMENCLATURE

A = preexponential factor
 Bi_H = biot number of heat transfer
 C_{sg} and C_{gs} = coefficients in turbulence model
 C_{μ} , $C_{1\epsilon}$, $C_{2\epsilon}$, and $C_{3\epsilon}$ = coefficients in turbulence model
 C_{pq} = heat capacity of q phase, $J/(kg \cdot K)$
 e_s = particle–particle restitution coefficient
 E_a = activation energy, $J/(kmol \cdot K)$
 d_p = particle diameter, m
 d_{pore} = pore diameter intraparticle, m
 D_e = mixed diffusion coefficient for CFD model, m^2/s
 D_{im} = the diffusion coefficient for single-particle model, m^2/s
 D_{ij} = the bulk diffusion coefficient of species i and j , m^2/s
 $D_{i,Kn}$ = Knudsen diffusion coefficient of species i , m^2/s
 D_q = diffusivities of the q phase
 g = gravitational acceleration, m/s^2
 g_0 = radial distribution function
 $G_{k,q}$ = generation of turbulence kinetic energy due to mean velocity gradient in the q phase
 hh_g = heat-transfer coefficient in the external of the catalyst, $W/(m^2 \cdot K)$
 h_{mf} = height of catalyst phase in the fluidized bed, m
 h_q = enthalpy of q phase, J/kg
 H_{sg} and H_{gs} = interphase exchange coefficient of energy, $W/(m^3 \cdot K)$
 I_{2D} = the second invariant of the deviator stress tensor
 \bar{I} = identity matrix
 k_1 , k_2 = kinetic parameters, $kmol/(m^3 \cdot s)$
 $k_{eff,q}$ = thermal coefficient of the q phase, $W/(m \cdot K)$
 k_q = turbulence kinetic energy tensor of the q phase

k_{Θ_s} = diffusion coefficient for granular energy
 kk_g = mass-transfer coefficient in the external of catalyst, m/s
 K_i = equilibrium constant parameters, MPa^{-1}
 K_{gs} and K_{sg} = interphase exchange coefficient of momentum, $kg/(m^3 \cdot s)$
 M = average molecule weight of all species, $kg/kmol$
 M_i = molecule weight of species i , $kg/kmol$
 M_{ij} = average molecule weight of species i and j , $kg/kmol$
 Nu = Nusselt number
 Nu_s = Nusselt number of the solid phase
 p = pressure, Pa
 p_s = particle-phase pressure, Pa
 P_i = partial pressure of species i , MPa
 Pr = Prandtl number
 r = coordinate inside a single particle, m
 Re_s = particle Reynolds number
 $R_{\epsilon,q}$ = addition term in ϵ equation of the q phase
 \mathcal{R}_i = rate of reaction i , $kmol/(m^3 \cdot s)$
 S = scalar measure of the deformation tensor
 Sc = Schmidt number
 Sh = Sherwood number
 T = temperature, K
 T^s = temperature on the outer surface of the catalyst, K
 Y_i = mass fraction of species i
 Y_i^s = mass fraction of species i in the external of catalyst
 \bar{u}_q = phase-weighted velocity, m/s
 \bar{v}_q = velocity of the q phase, m/s
 $\bar{v}_{dr,sg}$ = relative velocity between gas and solid, m/s

Greek Letters

α_q = volume fraction of the q phase
 γ_{Θ_s} = collision dissipation of energy
 ϵ_q = turbulence dissipation rate of the q phase, m^2/s^3
 ΔH_i = heat released by reaction i , $J/kmol$
 η = effectiveness factor
 θ = angle of internal friction, degree
 Θ_s = granular temperature, m^2/s^2
 λ_{eff} = effective thermal coefficient, $W/(m \cdot K)$
 λ_s = solid bulk viscosity, $Pa \cdot s$
 μ_g = gas viscosity, $Pa \cdot s$
 μ_s = solid shear viscosity, $Pa \cdot s$
 $\mu_{s,coi}$ = solid collision viscosity, $Pa \cdot s$
 $\mu_{s,kin}$ = solid kinetic viscosity, $Pa \cdot s$
 $\mu_{s,fr}$ = solid frictional viscosity, $Pa \cdot s$
 $\mu_{t,q}$ = turbulent viscosity of the q phase
 ρ_q = density of q phase, kg/m^3
 $(\sum_v)_i$ = diffusion volume of species i
 σ_q = turbulent Prandtl numbers for the q phase
 σ_{sg} and σ_{gs} = dispersion Prandtl number between gas and solid, 0.75
 $\bar{\tau}_q$ = shear stress, N/m^2
 ϕ_{gs} = energy exchange between gas and solid
 ψ = intraparticle porosity

Superscript

p = catalyst particle
 s = outer surface of the catalyst particle

■ REFERENCES

- (1) Gunjal, P. R.; Ranade, V. V. Modeling of laboratory and commercial scale hydro-processing reactors using CFD. *Chem. Eng. Sci.* **2007**, *62*, 5512–5526.
- (2) Lin, L.; Pan, P. B.; Zhou, Z. F.; Li, Z. J.; Yan, J. X.; Sun, M. L.; Yao, Y. G. Cu/SiO₂ catalysts prepared by the sol-gel method for

hydrogenation of dimethyl oxalate to ethylene glycol. *Chin. J. Catal.* **2011**, *32*, 957–969.

(3) Shoaiefar, P.; Abbasian, M.; Entezami, A. A. A convenient method for preparation of amphiphilic monomethoxypoly(ethylene glycol)-polystyrene diblock copolymer by NMRP technique. *J. Polym. Res.* **2007**, *14*, 45–52.

(4) UOPLLC. *Attrition resistant catalyst for light olefin production*. WO PCT 05952A2, 2002.

(5) Gao, X.; Zhu, Y. P.; Luo, Z. H. CFD modeling of gas flow in porous medium and catalytic coupling reaction from carbon monoxide to diethyl oxalate in fixed-bed reactors. *Chem. Eng. Sci.* **2011**, *66*, 6028–6038.

(6) Yin, A. Y.; Guo, X. Y.; Dai, W. L.; Fan, K. N. Effect of initial precipitation temperature on the structural evolution and catalytic behavior of Cu/SiO₂ catalysts in the hydrogenation of dimethyl oxalate to ethylene glycol. *Catal. Commun.* **2011**, *12*, 412–416.

(7) Yin, A. Y.; Qu, J. W.; Guo, X. Y.; Dai, W. L.; Fan, K. N. The influence of B-doping on the catalytic performance of Cu/HMS catalyst for the hydrogenation of dimethyl oxalate. *Appl. Catal., A* **2011**, *400*, 39–47.

(8) Wang, B. W.; Xu, Q.; Song, H.; Xu, G. H. Synthesis of methyl glycolate by hydrogenation of dimethyl oxalate over Cu-Ag/SiO₂ catalyst. *J. Nat. Gas Chem.* **2007**, *16*, 78–80.

(9) Yin, A. Y.; Wen, C.; Guo, X. Y.; Dai, W. L.; Fan, K. N. Influence of Ni species on the structural evolution of Cu/SiO₂ catalyst for the chemoselective hydrogenation of dimethyl oxalate. *J. Catal.* **2011**, *280*, 77–88.

(10) He, Z.; Lin, H. Q.; He, P.; Yuan, Y. Z. Effect of boric oxide doping on the stability and activity of a Cu-SiO₂ catalyst for vapor-phase hydrogenation of dimethyl oxalate to ethylene glycol. *J. Catal.* **2011**, *277*, 54–63.

(11) Levenspiel, O. *Chemical Reaction Engineering*; John Wiley & Sons: New York, NY, USA, 2002.

(12) Chai, C. J.; Zhang, G. L. *Chemical engineering fluid flows and heat transport*; Chemical Engineering Press: Beijing, China, 2004.

(13) Kang, W. G.; Zhang, B.; Li, W.; Xiao, W. D. Simulation of the reactor for dimethyl oxalate hydrogenation to ethylene glycol. *J. Nat. Gas Chem. Eng.* **2008**, *33*, 37–42 (in Chinese).

(14) Yin, A. Y.; Guo, X. Y.; Fan, K. N.; Dai, W. L. Influence of copper precursors on the structure evolution and catalytic performance of Cu/HMS catalysts in the hydrogenation of dimethyl oxalate to ethylene glycol. *Appl. Catal., A* **2010**, *377*, 128–133.

(15) Guo, X. Y.; Yin, A. Y.; Dai, W. L.; Fan, K. N. One pot synthesis of ultra-high copper contented Cu/SBA-15 material as excellent catalyst in the hydrogenation of dimethyl oxalate to ethylene glycol. *Catal. Lett.* **2009**, *132*, 22–27.

(16) Lin, L.; Pan, P. B.; Zhou, Z. F.; Li, Z. J.; Yan, J. X.; Sun, M. L.; Yao, Y. G. Cu/SiO₂ catalysts prepared by the sol-gel method for hydrogenation of dimethyl oxalate to ethylene glycol. *Chin. J. Catal.* **2011**, *32*, 957–969.

(17) Zhu, Y. Y.; Wang, S. R.; Zhu, L. J.; Ge, X. L.; Li, X. B.; Luo, Z. Y. The influence of copper particle dispersion in Cu/SiO₂ catalysts on the hydrogenation synthesis of ethylene glycol. *Catal. Lett.* **2010**, *135*, 275–281.

(18) Lin, J. D.; Zhao, X. Q.; Cui, Y. H.; Zhang, H. B.; Liao, D. W. Effect of feedstock solvent on the stability of Cu/Si₂ catalyst for vapor-phase hydrogenation of dimethyl oxalate to ethylene glycol. *Chem. Commun.* **2012**, *48*, 1177–1179.

(19) Yin, A. Y.; Wen, C.; Dai, W. L.; Fan, K. N. Ag/MCM-41 as a highly efficient mesostructured catalyst for the chemoselective synthesis of methyl glycolate and ethylene glycol. *Appl. Catal., B* **2011**, *108*, 90–99.

(20) Wang, S. R.; Li, X. B.; Yin, Q. Q.; Zhu, L. J.; Luo, Z. Y. Highly active and selective Cu/SiO₂ catalysts prepared by the urea hydrolysis method in dimethyl oxalate hydrogenation. *Catal. Commun.* **2011**, *12*, 1246–1250.

(21) Nijemeisland, M.; Dixon, A. G. CFD study of fluid flow and wall heat transfer in a fixed bed of spheres. *AIChE J.* **2004**, *50*, 906–921.

(22) Alwahabi, S. M.; Froment, G. F. Conceptual reactor design for the methanol-to-olefins process on SAPO-34. *Ind. Eng. Chem. Res.* **2004**, *43*, 5112–5122.

(23) Schoenfelder, H.; Hinderer, J.; Werther, J.; Keil, F. J. Methanol to olefins—Prediction of the performance of a circulating fluidized-bed reactor on the basis of kinetic experiments in a fixed-bed reactor. *Chem. Eng. Sci.* **1995**, *49*, 5377–5390.

(24) Di Blasi, C. Modeling chemical and physical processes of wood and biomass pyrolysis. *Prog. Energy Combust. Sci.* **2008**, *34*, 47–90.

(25) Singh, A.; Verma, R.; Kishore, K.; Verma, N. Multi-stage fluidized bed column: Hydrodynamic study. *Chem. Eng. Process.* **2008**, *47*, 957–970.

(26) Qian, W. H.; Liu, T.; Wang, Z. W.; Wei, F.; Li, Z. F.; Luo, G. H.; Li, Y. D. Production of hydrogen and carbon nanotubes from methane decomposition in a two-stage fluidized bed reactor. *Appl. Catal., A* **2004**, *260*, 223–228.

(27) McKenna, T. F.; Spitz, R.; Coklat, D. Heat transfer from catalysts with computational fluid dynamics. *AIChE J.* **1999**, *45*, 2392–2410.

(28) Solsvik, J.; Jakobsen, H. A. A numerical study of a two property catalyst/sorbent pellet design for the sorption-enhanced steam-methane reforming process: Modeling complexity and parameter sensitivity study. *Chem. Eng. J.* **2011**, *178*, 407–422.

(29) Cardoso, S. S. S.; Rodrigues, A. E. Convection, diffusion and reaction in a nonisothermal, porous catalyst slab. *AIChE J.* **2007**, *53*, 1325–1336.

(30) Saliccioli, M.; Stamatakis, M.; Caratzoulas, S.; Vlachos, D. G. A review of multiscale modeling of metal-catalyzed reactions mechanism development for complexity and emergent behavior. *Chem. Eng. Sci.* **2011**, *66*, 4319–4355.

(31) Kulkarni, K.; Moon, J.; Zhang, L. B.; Lucia, A.; Linninger, A. A. Multiscale modeling and solution multiplicity in catalytic pellet reactors. *Ind. Eng. Chem. Res.* **2008**, *47*, 8572–8581.

(32) Cornelissen, J. T.; Taghipour, F.; Escudié, R.; Ellis, N.; Grace, J. R. CFD modelling of a liquid-solid fluidized bed. *Chem. Eng. Sci.* **2007**, *62*, 6334–6348.

(33) Vaishali, S.; Roy, S.; Mills, P. L. Hydrodynamic simulation of gas-solids downflow reactors. *Chem. Eng. Sci.* **2008**, *63*, 5107–5119.

(34) Gao, J. S.; Lan, X. Y.; Fan, Y. P.; Chang, J.; Wang, G.; Lu, C. X.; Xu, C. M. CFD modeling and validation of the turbulent fluidized bed of FCC particles. *AIChE J.* **2009**, *55*, 1680–1694.

(35) Cao, C. Q.; Dong, S. Q.; Zhao, Y. A.; Guo, Q. J. Experimental and numerical research for fluidization behaviors in a gas-solid acoustic fluidized bed. *AIChE J.* **2010**, *56*, 1726–1736.

(36) Vaishali, S.; Roy, S.; Mills, P. L. Hydrodynamic simulation of gas-solids downflow reactors. *Chem. Eng. Sci.* **2008**, *63*, 5107–5119.

(37) Darelus, A.; Rasmuson, A.; van Wachem, B.; Björn, I. N.; Folestad, S. CFD simulation of the high shear mixing process using kinetic theory of granular flow and frictional stress models. *Chem. Eng. Sci.* **2008**, *63*, 2188–2199.

(38) Min, J.; Drake, J. B.; Heindel, T. J.; Fox, R. O. Experimental validation of CFD simulations of a lab-scale fluidized-bed reactor with and without side-gas. *AIChE J.* **2010**, *56*, 1434–1446.

(39) Mahecha-Botero, A.; Boyd, T.; Gulamhusein, A.; Comyn, N.; Lim, C. J.; Grace, J. R.; Shirasaki, Y.; Yasuda, I. Pure hydrogen generation in a fluidized bed membrane reactor: experimental findings. *Chem. Eng. Sci.* **2008**, *63*, 2752–2761.

(40) Mahecha-Botero, A.; Grace, J. R.; Lim, C. J.; Elnashaie, S. S. E. H. Pure hydrogen generation in a fluidized bed membrane reactor: application of the generalized comprehensive reactor model. *Chem. Eng. Sci.* **2009**, *64*, 3826–3835.

(41) Li, T. W.; Mahecha-Botero, A.; Grace, J. R. Computational fluid dynamic investigation of change of volumetric flow in fluidized-bed reactors. *Ind. Eng. Chem. Res.* **2010**, *49*, 6780–6789.

(42) Zhou, Z. Y.; Yu, A. B.; Zulli, P. Particle scale study of heat transfer in packed and bubbling fluidized beds. *AIChE J.* **2009**, *55*, 868–884.

- (43) Mahecha-Botero, A.; Grace, J. R.; Elnashaie, S. S. E. H.; Lim, C. J. Advances in modeling of fluidized-bed catalytic reactors: A comprehensive review. *Chem. Eng. Commun.* **2009**, *196*, 1375–1405.
- (44) Yan, W. C.; Luo, Z. H.; Lu, Y. H.; Chen, X. D. A CFD-PBM-PMLM integrated model for the gas-solid flow fields in fluidized bed polymerization reactors. *AIChE J.* **2012**, *58*, 1717–1732.
- (45) Bi, H. T.; Li, J. H. Multiscale analysis and modeling of multiphase chemical reactors. *Adv. Powder Technol.* **2004**, *15*, 607–627.
- (46) Dollet, A. Multiscale modeling of CVD film growth—A review of recent works. *Surf. Coat. Technol.* **2004**, *177–178*, 245–251.
- (47) Li, J. H.; Kwauk, M. Exploring complex systems in chemical engineering—The multi-scale methodology. *Chem. Eng. Sci.* **2003**, *58*, 521–535.
- (48) Wang, W.; Li, J. H. Simulation of gas-solid two-phase flow by a multi-scale CFD approach—Extension of the EMMS model to the sub-grid level. *Chem. Eng. Sci.* **2007**, *62*, 208–231.
- (49) Hughes, T. J. R.; Feijoo, G. R.; Mazzei, L.; Quincy, J. B. The variational multiscale method—A paradigm for computational mechanics. *Comput. Methods Appl. Mech. Eng.* **1998**, *166*, 3–24.
- (50) Guardo, A.; Casanovas, M.; Ramírez, E.; Recasens, F.; Magaña, I.; Martínez, D.; Larrayoz, M. A. CFD modeling on external mass transfer and intra-particle diffusional effects on the supercritical hydrogenation of sunflower oil. *Chem. Eng. Sci.* **2007**, *62*, 5954–5061.
- (51) Aris, R. *The Mathematical Theory of Diffusion and Reaction in Permeable Catalysts*; Oxford, Clarendon, Oxford, U. K., 1975.
- (52) Lopes, J. C. B.; Dias, M. M.; Mata, V. G.; Rodrigues, A. E. Flow field and non-isothermal effects on diffusion, convection and reaction in permeable catalysts. *Ind. Eng. Chem. Res.* **1995**, *34*, 148–157.
- (53) Wang, G.; Coppens, M. O. Rational design of hierarchically structured porous catalysts for autothermal reforming of methane. *Chem. Eng. Sci.* **2010**, *65*, 2344–2352.
- (54) Rout, K. R.; Solsvik, J.; Nayak, A. K.; Jakobsen, H. A. A numerical study of multicomponent mass diffusion and convection in porous pellets for the sorption-enhanced steam methane reforming and desorption processes. *Chem. Eng. Sci.* **2011**, *66*, 4111–4126.
- (55) Solsvik, J.; Jakobsen, H. A. Modeling of multicomponent mass diffusion in porous spherical pellets: Application to steam methane reforming and methanol synthesis. *Chem. Eng. Sci.* **2011**, *66*, 1986–2000.
- (56) Wilke, C. R. Diffusional properties of multicomponent gases. *Chem. Eng. Prog.* **1950**, *46*, 95–104.
- (57) Jackson, R. *Transport in porous catalysts*; Elsevier: Amsterdam, The Netherlands, 1977.
- (58) Mason, E. A.; Malinauskas, A. P. *Gas transport in porous media: The Dusty gas model*; Elsevier: Amsterdam, The Netherlands, 1983.
- (59) Burghardt, A.; Aerts, J. Pressure changes during diffusion with chemical reaction in porous pellet. *Chem. Eng. Process* **1988**, *23*, 77–87.
- (60) Graaf, G. H.; Scholtens, H.; Stamhuis, E. J.; Beenackers, A. A. C. M. Intra-particle diffusion limitations in low-pressure methanol synthesis. *Chem. Eng. Sci.* **1990**, *45*, 773–783.
- (61) Elnashaie, S. S. E. H.; Abashar, M. E. E. Steam reforming and methanation effectiveness factors using the dusty gas model under industrial conditions. *Chem. Eng. Process.* **1992**, *32*, 177–189.
- (62) Salmi, T.; Wärnå, J. Modelling of catalytic packed-bed reactors—comparison of different diffusion models. *Comput. Chem. Eng.* **1991**, *15*, 715–727.
- (63) Wesenberg, M. H.; Svendsen, H. F. Mass and heat transfer limitations in a heterogeneous model of a gas-heated steam reformer. *Ind. Eng. Chem. Res.* **2007**, *46*, 667–676.
- (64) Rusten, H. K.; Ochoa-Fernández, E.; Lindborg, H.; Chen, D.; Jakobsen, H. A. Hydrogen production by sorption-enhanced steam methane reforming using lithium oxides as CO₂-acceptor. *Ind. Eng. Chem. Res.* **2007**, *46*, 8729–8737.
- (65) Ibashi, W.; Groppi, G.; Forzatti, P. Kinetic measurements of CH₄ combustion over a 10% PdO/ZrO₂ catalyst using an annular flow microreactor. *Catal. Today* **2003**, *83*, 115–129.
- (66) Fabiano, A.; Fernandes, N.; Liliane, M.; Lona, F. Heterogeneous modeling of fluidized bed polymerization reactors, Influence of mass diffusion into the polymer particle. *Comput. Chem. Eng.* **2002**, *26*, 841–848.
- (67) Zhu, Y. P. The multi-scale CD model of gas-solid catalytic fluidized bed reactor and the simulation in two classical reaction systems. Master Dissertation, Xiamen University: Xiamen, China, 2013.
- (68) Yin, A. Y.; Dai, W. L.; Fan, K. N. Thermodynamics of ethylene glycol synthesis via hydrogenation of dimethyl oxalate. *Petrochem. Technol.* **2008**, *37*, 62–66.
- (69) Zhang, Q. Y.; Huang, W. J.; Wen, F.; Xiao, W. D. Hydrogenation of dimethyl oxalate to ethylene glycol. *Petrochem. Technol.* **2007**, *36*, 340–344.
- (70) Lun, C. K. K.; Savage, S. B.; Jeffrey, D. J.; Chepurny, N. Kinetic theories for granular flow-inelastic particles in couette-flow and slightly inelastic particles in a general flow field. *J. Fluid Mech.* **1984**, *140*, 223–232.
- (71) Ding, J.; Gidaspow, D. A bubbling fluidization model using kinetic-theory of granular flow. *AIChE J.* **1990**, *36*, 523–538.
- (72) Wachem, B. G. M.; Schouten, J. C.; Krishna, R.; Bleek, C. M. V.; Sinclair, J. L. Comparative analysis of CFD models of dense gas-solid systems. *AIChE J.* **2001**, *6*, 1035–1051.
- (73) Chen, X. Z.; Shi, D. P.; Gao, X.; Luo, Z. H. A fundamental CFD study of the gas-solid flow field in fluidized bed polymerization reactors. *Powder Technol.* **2011**, *205*, 276–288.
- (74) Gidaspow, D. *Multiphase flow and fluidization: Continuum and kinetic theory descriptions*; Academic Press: Boston, 1994.
- (75) Gunn, D. J. Transfer of heat or mass to particles in fixed and fluidized beds. *Int. J. Heat Mass Transfer* **1978**, *21*, 467–475.
- (76) Bradshaw, P.; Cebeci, T.; Whitelaw, J. H. *Engineering calculation methods for turbulent flow*; Academic Press: London, 1981.
- (77) Chen, C. J.; Jaw, S. Y. *Fundamentals of turbulence modeling*; Taylor & Francis: Abingdon, U.K., 1998.
- (78) Jiang, C. W.; Zheng, Z. W.; Zhu, Y. P.; Luo, Z. H. Design of a two-stage fluidized bed reactor for preparation of diethyl oxalate from carbon monoxide. *Chem. Eng. Res. Des.* **2012**, *90*, 915–925.
- (79) Wang, J. W. A review of Eulerian simulation of Geldart A particles in gas-fluidized beds. *Ind. Eng. Chem. Res.* **2009**, *48*, 5567–5577.
- (80) Singh, A.; Verma, R.; Kishore, K.; Verma, N. Multi-stage fluidized bed column: Hydrodynamic study. *Chem. Eng. Process.* **2008**, *47*, 957–970.
- (81) Romeo, L. M.; Diez, L. I.; Guedea, I.; Bolea, I.; Lupianez, C.; Gonzalez, A.; Pallares, J.; Teruel, E. Design and operation assessment of an oxyfuel fluidized bed combustor. *Exp. Therm. Fluid Sci.* **2011**, *35*, 477–484.